Insights into sulfur and hydrogen sulfide induced corrosion of sintered nanocopper paste A combined experimental and ab initio study

Chen, Wei; Liu, Xu; Yang, Zhoudong; Liu, Xu; Hu, Dong; Zhu, Xi; Fan, Xuejun; Zhang, Guoqi; Fan, Jiajie

DOI
10.1016/j.matdes.2024.112876

Publication date
2024

Document Version
Final published version

Published in
Materials and Design

Materials & Design 240 (2024) 112876

Contents lists available at ScienceDirect

Materials & Design

journal homepage: www.elsevier.com/locate/matdes

Insights into sulfur and hydrogen sulfide induced corrosion of sintered nanocopper paste: A combined experimental and ab initio study

Wei Chen [a], Xu Liu [a], Zhoudong Yang [a], Dong Hu [b], Xu Liu [b], Xi Zhu [a,c], Xuejun Fan [d], Guoqi Zhang [b], Jiajie Fan [a,b,c,*]

[a] Institute of Future Lighting, Academy for Engineering & Technology, Shanghai Engineering Technology Research Center for SiC Power Device, Fudan University, Shanghai 200433, China
[b] EEMCS Faculty, Delft University of Technology, Delft 2628, the Netherlands
[c] Research Institute of Fudan University in Ningbo, Ningbo 315336, China
[d] Department of Mechanical Engineering, Lamar University, PO Box 10028, Beaumont, TX 77710, USA

ARTICLE INFO

Keywords:
Sintered nanocopper
Atmospheric corrosion
Sulfur and hydrogen sulfide
Density functional theory

ABSTRACT

The power semiconductor joining technology through sintering of copper nanoparticles is well-suited for die attachment in wide bandgap (WBG) semiconductors, offering high electrical, thermal, and mechanical performances. However, sintered nanocopper will be prone to degradation resulting from corrosion in sulfur-containing corrosive environments such as offshore areas. In this study, experiments, including aging test and corrosion characterization, and simulations based on density functional theory (DFT) studies were conducted to explore the corrosion behavior and mechanism of elemental sulfur (S_8) and hydrogen sulfide (H_2S) on sintered nanocopper. The experimental results indicated that loose corrosion products were observed on the sintered nanocopper during the ageing process involving S_8, and compact layered corrosion products formed during the ageing process involving H_2S. Furthermore, similar corrosion product compositions (Cu_2O, Cu_2S, CuO, CuS, and potentially Cu_2SO_4 or $CuSO_4$) were observed in both the S_8- and H_2S-ageing processes. However, the S_8-ageing process exhibited more noticeable corrosion penetration. This was explained in simulations results: the unsaturated Cu sites on the oxide layer [$Cu_2O(1\,1\,1)$] of the sintered nanocopper could adsorb both H_2S and S_8, while the saturated Cu sites only exhibited the potential to adsorb S_8.

1. Introduction

Silicon carbide (SiC) is a kind of wide bandgap (WBG) semiconductor material, SiC dies offer significant advantages in terms of high-temperature resistance, enhanced energy efficiency, and elevated switching frequency for power devices [1–3]. These devices have found extensive applications in various domains [4,5], including new energy vehicles and renewable energy generation/storage. However, at present, two critical issues persist, impeding the broader adoption of SiC-based electronics in demanding environments such as offshore areas. First, conventional tin-based solder, as a die-attachment material, cannot meet the high-temperature durability requirements of SiC [6,7]. Then, in corrosive environments containing sulfur, electronic devices are susceptible to degradation caused by corrosion [8–10].

Electronic devices operating in ambient air will be inherently susceptible to corrosion from factors such as humidity, oxygen, corrosive gases, dust, and pollutants. This will be especially evident in challenging environments such as coastal and offshore areas [11,12] with high salt levels and corrosive gases containing S, such as S_8 and H_2S. Similarly, facilities such as mines, paper mills, wastewater/garbage treatment plants, farms, and fertilizer factories exposed to high pollutant concentrations will face heightened corrosion risks [13,14].

The corrosion behaviors of sintered silver under outage and voltage bias conditions have been extensively investigated in different environments, including air, electrolyte, and corrosive gases. The corrosion study of sintered Ag under outage conditions is firstly introduced. C.T. Chen et al. [15] conducted a 1000 h high-temperature ageing study at 250 °C in ambient air on sintered Ag. They observed that ageing leads to a coarsening of the microstructure of the sintered silver. However, the ageing process does not significantly affect the shear strength of the joints. E. Kolbinger et al. [16] conducted research on the corrosion behaviors of sintered Ag with varying sintering pressures in artificial

* Corresponding author.
E-mail address: jiajie_fan@fudan.edu.cn (J. Fan).

https://doi.org/10.1016/j.matdes.2024.112876
Received 13 October 2023; Received in revised form 9 January 2024; Accepted 21 March 2024
Available online 24 March 2024

seawater and found that higher sintering pressures resulted in reduced corrosion degree of the sintered Ag. H. Gong et al. [17] demonstrated that the shear strength of sintered Ag joints significantly decreases with the increase in ageing time in a 3 % NaCl solution at 50 °C. D. Hu et al. [18] conducted experiments and simulations to determine the corrosion process of sintered Ag by S_8 vapor. The researchers found that higher temperatures accelerated sulfidation, while increased humidity inhibited sulfidation reactions. The simulations also showed that S_8 had a greater propensity for penetrating the porous structure of sintered Ag compared to solid bulk Ag.

Next, the corrosion study of sintered Ag under voltage bias conditions is presented, wherein sintered Ag mainly experiences corrosion characterized by Ag migration. The corrosion behavior of sintered Ag on aluminum oxide substrates was also investigated by G.Q. Lu et al. [19,20], and the study showed that applying a voltage of 50 V to the sintered silver electrodes in dry air resulted in the formation of Ag migration dendrites at temperatures above 250 °C. Interestingly, within the temperature range of 250–400 °C, Ag dendrites grew from the anode to the cathode, while at 500 °C, dendritic growth was reversed, occurring from the cathode to the anode. The presence of oxygen was identified as a crucial factor in facilitating Ag migration in dry air. They also [21] used the thin electrolyte layer (TEL) method to investigate the corrosion behavior of sintered silver electrodes under a voltage bias of 3 V in NaCl solutions with different concentrations. The study found that increasing the NaCl concentration led to longer short-circuiting times of the silver electrodes. In addition, mechanistic analysis [22] revealed that in low-concentration electrolytes, silver dendrites, and cloud-like Ag_2O precipitates formed, while high-concentration electrolytes hindered Ag_2O formation, resulting in the presence of more Ag elements as dendrites. At higher concentrations, limited Ag^+ ions would combine with Cl^- to form AgCl, depositing on the anode and impeding further dissolution. D. Minzari et al. [23] found corrosion in power modules used in pig farms, particularly in sintered contact pads. The corrosion was caused by sulfur-containing corrosive gases penetrating the silicone gel layer, leading to the growth of Ag_2S dendrites on the pad edges under a bias voltage of 450 V. Furthermore, some studies have also reported methods to mitigate Ag migration. Riva et al. [24] applied a 20-μm parylene coating on sintered Ag electrodes and aluminum oxide surfaces, effectively mitigating Ag migration. In addition, Wang et al. [25] and D. Li et al. [26] introduced Pd and Si nanoparticles into nano Ag paste, respectively, to enhance resistance against migration in sintered silver. In the studies, Pd and Si demonstrated preferential reactivity with Ag over O_2.

Due to its relatively recent development, the current research on sintered Cu primarily focuses on enhancing its initial performance [27,28], with limited attention given to its corrosion properties. The following section will present the corrosion behavior and protection methods of bulk copper. T.T.M. Tran et al. [29] conducted corrosion experiments on copper samples in an H_2S-containing gas environment, with the analysis of the corrosion products revealing the predominant formation of Cu_2O, Cu_2S, and a small amount of CuO. The concentration of H_2S, temperature, and humidity accelerated the production of corrosion products, with Cu_2O showing greater sensitivity to humidity compared to Cu_2S. T.N. Wassermann et al. from Infineon [30] discovered that under high humidity, high voltage, and H_2S environmental conditions, Cu dendritic growth occurred between DBC Cu electrodes, with the dendrites growing from the anode toward the cathode direction. Methods to mitigate corrosion in bulk Cu have also been reported in some studies. Tang et al. [31] also synthesized polyvinylbutyral anticorrosive coatings with SnS nanosheets, and found that incorporating 0.1 wt% SnS nanosheets provided optimal corrosion protection for Cu substrates. Using density functional theory (DFT) and reactive force field (ReaxFF) simulations, D. Kumar et al. [32] investigated the corrosion inhibition mechanism of imidazole, adenine, and purine on Cu. The study demonstrated the formation of stable chemical bonds between the Cu atoms and the adsorbed N atoms, highlighting the underlying mechanism of corrosion inhibition.

Despite extensive research on the corrosion phenomena and protection strategies involving S in sintered Ag, the corrosion mechanisms of S_8 or H_2S for sintered Cu have not been clearly elucidated. In this study, the corrosion phenomena and products of sintered Cu induced by S_8 or H_2S were experimentally investigated. Subsequently, the adsorption characteristics of S_8 or H_2S on the Cu_2O oxide layer of sintered Cu were explored using DFT simulation.

2. Experimental details

2.1. Sample preparation

The Cu quasi-nanoparticles (QNPs) synthesized using the physical vapor deposition (PVD) method were selected as the raw materials in this study. The Cu QNPs were nearly spherical in shape and 150–300 nm in diameter, as shown in Fig. 1(a). The Cu QNPs were treated with carboxylic acids (99.0 %, Aladdin Reagent Co., Ltd.) to remove Cu oxide. After treatment, a nanometer-thick coating layer of reducing substance formed on the particle surfaces, as shown in Fig. 1(b).

To investigate the corrosion mechanism, 5 x 5 x 1 cm^3 sintered Cu plates were prepared. Fig. 2 shows the sample preparation process, which consisted of the following steps. (1) The Cu QNP paste and sintering mold were first prepared. The Cu QNP paste consisted of Cu QNPs, ethylene glycol (99.5 %, from Aladdin Reagent Co., Ltd.), and terpinol (95.0 %, from Aladdin Reagent Co., Ltd.), while the mold was composed of 304 stainless steel and consisted of a baseplate, square hole plate, and pressure block. (2) A certain amount of Cu QNP paste was injected into the mold. (3) The mold containing Cu QNP paste was then heated in a vacuum oven (DZF-6012, YIHENG) at 120 °C for 30 min, (4) and subjected to pressure-assisted sintering at a temperature of 250 °C and pressure of 20 MPa for 25 min, using the industrial standard sintering machine (Sinterstar Innovate-F-XL, Boschman) [see Fig. 2(b)]. (5) Samples were obtained after well-controlled laser cutting, and Fig. 1(c) and (d) depict the surface and cross-sectional morphologies of the sintered sample, indicating its highly dense and robust structure. Based on Fig. 1(d), the porosity of the sintered sample was quantified as 9.3 % calculated by image processing software (Fiji ImageJ, National Institutes of Health).

2.2. Experiment setup

In order to assess the impact of S_8 or H_2S on the corrosion of the sintered Cu QNP samples, this study employed two distinct ageing conditions, namely, (1) 100 °C + 100 % relative humidity (RH) + S_8

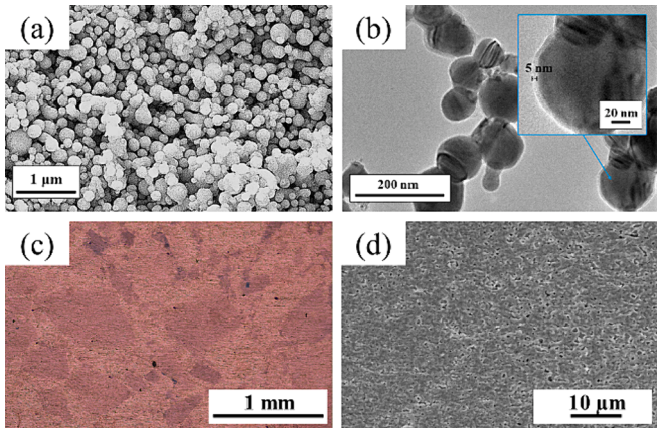

Fig. 1. Morphology characterization of the Cu QNPs and sintered sample: (a) SEM image of the Cu QNPs [33]; (b) transmission electron microscope (TEM) image of the Cu QNPs [33]; (c) surface image of the sintered sample; (d) cross-section image of the sintered sample.

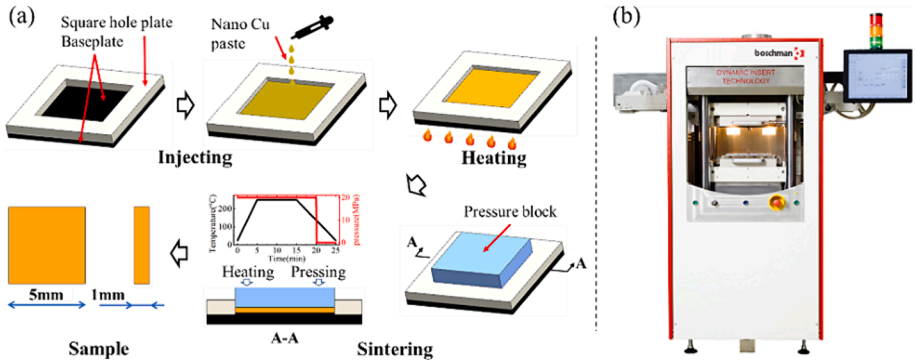

Fig. 2. (a) Schematic diagram depicting the sample sintering preparation process and (b) sintering machine.

vapor ageing and (2) 45 °C + 85 %RH + 100 ppb H_2S ageing. The setup for the 100 °C + 100 % RH + S_8 vapor ageing condition is illustrated in Fig. 3(a). In this setup, 30 mL of deionized water and 10 g of chemically pure S_8 were added to a 150-mL PTFE sealed tank, and a glass beaker containing the sintered samples was placed inside the sealed tank. A metal fixture was then used to securely clamp the sealed tank, ensuring a gas-tight seal. To create the 100 % RH condition with S_8 vapor, a high temperature of 100 °C was applied to the setup. During the ageing, 5 sintered samples were removed every 168 h, As shown in Fig. 3(b), ageing at 45 °C + 85 %RH + 100 ppb H_2S was conducted in a commercial gas corrosion test chamber (GH-180, YAMASAKI). All samples were retrieved upon completion of the test.

2.3. Characterization methodology

2.3.1. Morphology characterization

To examine the evolutionary changes in the macrotopography characteristics, the surface information of the sintered samples before and after ageing was captured using an optical microscope (OM) (BX53M, OLYMPUS). The microtopography and elemental composition of the corrosion products were then observed and analyzed using scanning electron microscopy with energy dispersive X-ray spectroscopy (SEM/EDS) (SU8010, HITACHI).

2.3.2. Crystallography analysis

To further analyze the corrosion product composition, the crystal structure changes in the sintered samples were characterized by an X-ray diffractometer (XRD) (D8, BRUKER) with Cu Kα radiation (λ = 0.15418 nm). MDI Jade was utilized to analyze the XRD test data.

2.3.3. Chemical elemental analysis

The chemical states of the elements present in the corrosion products were investigated by X-ray photoelectron spectroscopy (XPS) (Axis Supra+, SHIMADZU) equipped with an Al Kα excitation source (hv = 1486.6 eV). Thermo Avantage was utilized for the XPS spectrum deconvolution.

2.3.4. Mechanical properties analysis

The mechanical properties of the sintered samples before and after ageing were compared by a nanoindentation test system (iNano, KLA).

2.4. DFT simulation details

In this study, the interatomic behavior between different atoms was calculated using DFT implemented in Materials Studio (Accelrys, Inc.). The Perdew-Burke-Ernzerhof (PBE) function with the generalized gradient approximation (GGA) method was used to describe the exchange–correlation energy [34]. Core electron relativity effects were considered by using the all-electron method. Brillouin-zone integration was performed on a 2 × 2 × 1 k-point grid, which was generated automatically using the Monkhorst-Pack method [35]. During the calculation process, the electronic self-consistent field (SCF) convergence threshold was set to 2E − 6 eV, and a smearing value of 0.01 Ha was chosen to enhance SCF convergence. Additionally, the energy convergence tolerance, maximum force, and maximum displacement were set to 1E − 5 Ha, 0.002 Ha/Å, and 0.005 Å, respectively. Geometry optimization was performed using the $DMoL^3$ module with double numerical basis sets, including the polarization functions (DNP) and basis file 4.4. Charge density difference (CDD), charge difference (CD), and density of states (DOS) analyses were conducted using the CASTEP module, with a plane wave basis set.

To quantitatively access the interaction strength between S_8 or H_2S and $Cu_2O(1\,1\,1)$, the adsorption energy (E_{ads}) was calculated by the following equation [34,36]:

$$E_{ads} = E_{slab+gas} - E_{slab} - E_{gas} \quad (1)$$

where $E_{slab\ +\ gas}$, E_{slab}, and E_{gas} denote the total energies of $Cu_2O(1\,1\,1)$ with gas adsorption, clean $Cu_2O(1\,1\,1)$, and isolated gas molecules, respectively.

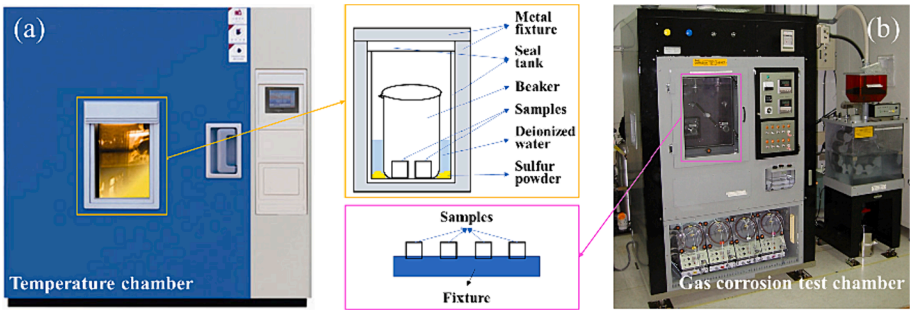

Fig. 3. Accelerated ageing test setup diagrams: (a) 100 °C + 100 %RH + S_8 and (b) 45 °C + 85 %RH + 100 ppb H_2S.

3. Results and discussions

In this section, the corrosion behavior of the sintered nanocopper induced by S_8- or H_2S-ageing was assessed by OM and SEM/EDS. Subsequently, the compositions of the corrosion products that formed under the two ageing conditions were explored by XRD/XPS. Then, the mechanical performance changes of the two aged samples were analyzed by nanoindentation. Finally, the corrosion mechanisms of S_8- or H_2S-ageing on sintered Cu was explored by DFT simulations.

3.1. Corrosion processes analysis

3.1.1. S_8-ageing corrosion

The corrosion behavior of the sintered samples during S_8-ageing was first analyzed using OM. Fig. 4 illustrates the temporal evolution of the macroscopic surface morphology of the sintered samples following the S_8-ageing process. Based on Fig. 4(a)–(h), it can be deduced that the corrosion of the sample could be divided into three distinct stages.

Stage I, known as the reaction controlled rapid corrosion stage, occurred from 0 to 96 h [see Figs. (a) to (e)]. During this stage, with the progression of ageing time, the unevenly distributed corrosion products gradually covered the sintered sample surface, leading to complete coverage. Simultaneously, the colour of the sample transformed from its original reddish-brown colour to black.

Stage II, referred to diffusion controlled slow corrosion stage, occurred from 96 to 144 h [see Figs. (e) to (g)]. During this stage, the corrosion rate was significantly reduced due to the coverage of corrosion products on the sample surface, which hindered the penetration of corrosive agents. At 144 h of corrosion, a slight detachment of corrosion products could also be observed in the area enclosed by the red circle in Fig. 4(g). The surface of the sample remained black in this stage.

Stage III, called the corrosion product detachment stage, occurred from 144 to 168 h [see Figs. (g) to (h)]. Due to the loose structure of the corrosion products, the accumulated corrosion products gradually partially detached from the corroded surface. As a result, the colour on the surface of the sintered sample changed from black to an alternating distribution of black and reddish-brown colour. It should be noted that while corrosion products are detaching, the surface of the sintered sample continues to undergo corrosion.

The weight loss method was used to characterize the mass of the corrosion products, which involved the following steps. (1) A balance (CP214, OHAUS) was used to measure the weight of the aged sintered sample. (2) For ultrasonic cleaning, an ultrasonic cleaning instrument (YA008G, YUNYI) was employed, and the aged sintered sample underwent a 20-min ultrasonic cleaning process. This step helped to eliminate corrosion products from the sample surface. (3) Then, the cleaned sample was placed in a temperature-controlled oven for drying, and dried at 60 °C for 30 min to remove any residual moisture within the sample. (5) Then the samples were weighed again, once the dried sample had cooled, using the balance to measure the weight. The difference in mass between pre- and post-cleaning represented the mass of the corrosion products.

Fig. 5 presents the variations in corrosion product mass over time. To ensure data consistency, repeated testing was conducted on the five samples at each time point. By linear fitting the data, the relationships between the mass of corrosion products and time in both Stages I and II could be obtained:

$$InstageI : y = 0.3733 + 0.04759x \quad (2)$$

$$InstageII : y = 2.2 + 0.2685x, \quad (3)$$

where x and y denote the corrosion ageing time (h) and the mass of the corrosion products per unit area (mg/cm^2), respectively. According to Eq. (2), it was inferred that the mass of the corrosion products per unit area for the aged sample at 168 h was 8.37 mg/cm^2, assuming rapid corrosion and no detachment occurred.

In Stage I, the mass of the corrosion products rapidly increased proportionally with the corrosion time. However, in Stage II, the accumulation rate of the corrosion products gradually decreased. The slope of the fitted curve in Stage II decreased from 0.04759, which was the same as that in Stage I, to 0.02685, representing a decrease rate of 43.58 %. Additionally, in Stage III, the mass of the corrosion products actually decreased, due to the detachment of the corrosion products. The variation in the corrosion products mass further confirms the rationality of dividing the corrosion process into 3 Stages.

The surface microstructural characteristics of the 168 h aged sample were analyzed by SEM, and the results are shown in Fig. 6(a)–(c). Three distinct microstructural features were observed on the corroded sample surfaces: (1) densely packed multi-faceted cone-shaped crystals, as shown in Fig. 6(a), (2) loosely arranged rod-like amorphous structures, as shown in Fig. 6(b), and (3) loosely arranged multi-faceted prism-shaped crystals, as presented in Fig. 6(c). EDS analysis was performed on the selected points within the three features, as indicated in Fig. 6(a)–(c), and the test results are summarized in Table 1. All three points exhibited a relatively higher proportion of O and Cu elements. The S

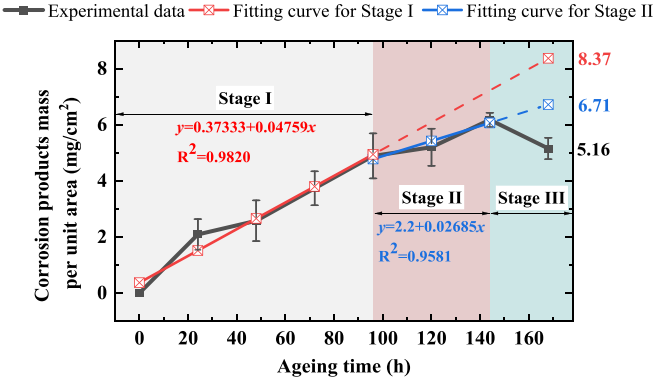

Fig. 5. Variations in corrosion product mass over S_8-ageing time.

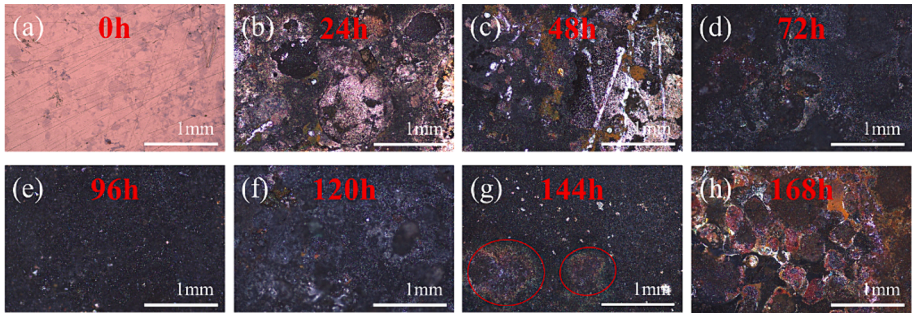

Fig. 4. Surface morphology evolution with corrosion S_8-ageing time.

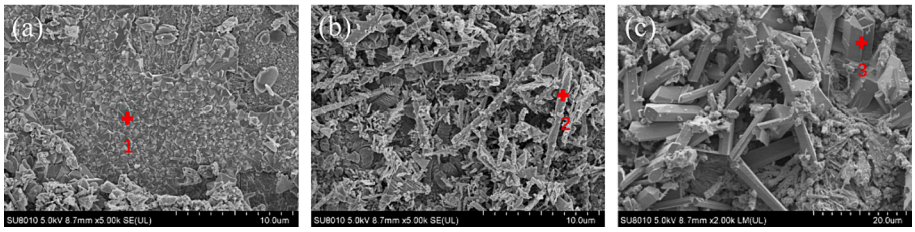

Fig. 6. The surface microstructural characteristics for the 168-h S_8 aged sample: (a) feature 1; (b) feature 2; (c) feature 3.

Table 1
Surface elemental composition in the different regions of the 168-h S_8-aged sample.

Point	Cu (at%)	O (at%)	S (at%)
1	59.6	39.47	0.93
2	55.21	16.49	28.3
3	21.33	70.57	8.1

content values at Points 2 and 3 were 28.3 % and 8.1 %, respectively, while Point 1 exhibited an extremely lower S content of only 0.93 %. Hence, we concluded that Feature 1 predominantly consisted of Cu-O compounds, while Features 2 and 3 indicated the presence of both Cu-O and Cu-S compounds, which led to further inference. During the ageing process of S_8, the surface of the sintered Cu underwent initial oxidation, resulting in the formation of Cu-O compounds. Subsequently, the Cu-O compounds reacted with S_8, resulting in the formation of loosely packed mixtures composed of Cu-O and Cu-S compounds.

To evaluate the depth of corrosion penetration in the sintered samples during S_8-ageing, resin embedding followed by metallographic grinding was employed to obtain the cross-sectional profiles of the 168-h aged samples. The process of preparing cross-section samples will disrupt the corrosion product layer on the sintered sample surface. These cross-sectional profiles were subsequently analyzed by SEM/EDS to observe the internal structure and elemental composition of the samples. As shown in Fig. 7(a), the sample surfaces exhibited varying degrees of corrosion, with the presence of severe corrosion-induced pits. The areas beneath these pits appeared darker in colour, indicating deeper corrosion penetration.

Additional analysis was conducted on the selected regions on the sample surface, including the pit region (Regions 1 and 2) and smooth region (Region 3), as shown in Fig. 7(a). The SEM magnified images corresponding to Region 1, Region 2, and Region 3 are depicted in Fig. 7 (b), (c), and (d), respectively. In Region 1, positions located at a distance of 10 μm from the surface displayed extensive darker regions, which became more uniform in colour with extension in the deeper region, distinguishing it from Regions 2 and 3. According to the marked positions in the figures, specific points were chosen within each region for elemental analysis, and the results are presented in Table 2. In Region 1, a small amount of S was observed, while S was not detected in Region 2. Within the corroded crater region, S extended into the sample to a depth of approximately 10 μm, as shown in Fig. 7(b). In Region 3, the absence of S implied that within the smooth region of the corroded surface, the depth of S penetration was shallow or the quantity of S penetration was minimal, rendering it insufficient for detection. Notably, the O content in Region 1 was noticeably higher than in Regions 2 and 3, providing further evidence that sulfidation reactions occurred following the oxidation reactions.

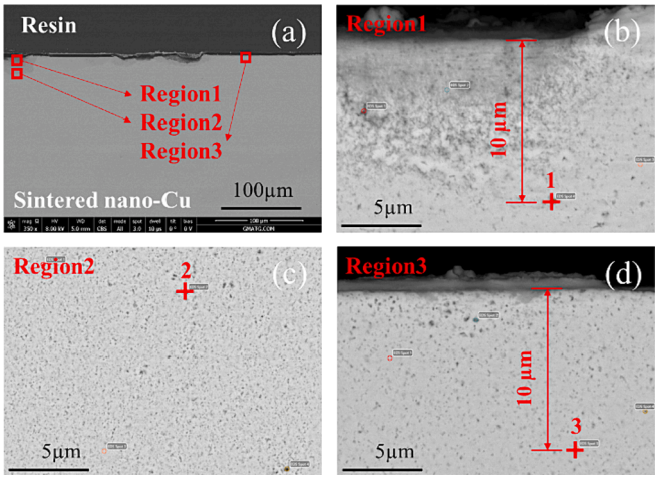

Fig. 7. Cross-sectional images of the 168-h S_8-aged sintered samples: (a) overall image, (b) magnified image of Region 1, (c) magnified image of Region 2, and (d) magnified image of Region 3.

3.1.2. *H_2S-ageing corrosion*

Fig. 8 shows the surface morphologies of the unaged and 168-h H_2S-aged sintered samples. As shown in Fig. 8(a) and (b), the colour of the sample transformed from its original colour of reddish-brown to a purple-green, following 168 h of H_2S ageing. The surface of the sample was coated with a layer of corrosion products, as depicted in Fig. 8(b). Notably, this corrosion product layer exhibited a distinct wrinkled morphology, which was characterized by numerous protrusions. This phenomenon could be attributed to the lower density of the corrosion products compared to the substrate material, low density implies the forming of more corrosion products. As the corrosion products accumulated and their volume increased, the accumulated stress eventually exceeded the adhesive strength between the corrosion products and the sample surface, resulting in detachment of the corrosion products from the surface [see Fig. 8(c)]. This detachment resulted in the observed wrinkled and protruded morphology on the surface. Utilizing the weight loss method, the average value of the unit mass of corrosion products for a set of 13 samples subjected to 168 h of H_2S-ageing was calculated to be 1.32 mg/cm^2, with a corresponding variance of 0.108.

SEM analysis was used to investigate the microstructural characteristics of the corroded sample surfaces, as presented in Fig. 8(c). The SEM image revealed the presence of layered corrosion products on the H_2S-aged sintered sample surface, with localized areas showing partial detachment of the laminar corrosion product layer from the underlying substrate. A similar detachment phenomenon was observed in Ref. [37] and Ref. [38]. EDS analysis was performed on the exposed sintered nanocopper substrate, corresponding to Region 1 in Fig. 8(b), and the intact corrosion product layer, corresponding to Region 2 in Fig. 8(b). The EDS analysis results are presented in Table 3, which showed that both Regions 1 and 2 contained O elements, while Region 1 exhibited

Table 2
Cross-section elemental compositions for the different regions of the 168-h S_8-aged sample.

Point	Cu (at%)	O (at%)	S (at%)
1	74.89	25.04	0.07
2	97.12	2.88	0.00
3	98.73	1.27	0.00

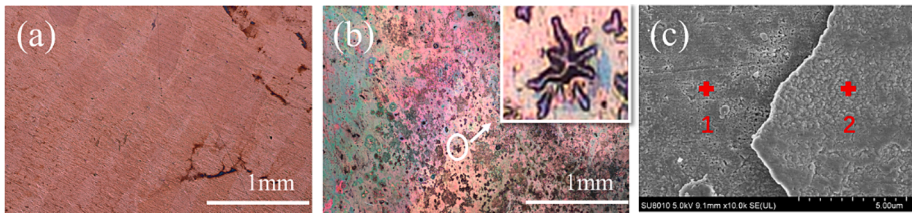

Fig. 8. The surface morphologies of the sintered sample: (a) macroscopic OM view of the unaged sintered sample, (b) macroscopic OM view of the 168-h H_2S-aged sample, and (c) microscopic SEM view of the 168-h H_2S-aged sample. The area revealed after the detachment of the corrosion film was labeled as "region 1", while the region containing the corrosion film was labeled as "region 2".

Table 3
EDS analysis results of the exposed sintered nanocopper substrate and corrosion product layer subjected to 168-h H_2S-ageing.

Region	Cu (at%)	O (at%)	S (at%)
1	71.54	28.46	0.00
2	62.06	14.06	23.93

significantly higher O content compared to Region 2. Notably, S elements were not detected in Region 1, while Region 2 exhibited substantial sulfur content of 23.93 at%. These findings supported the conclusion that similar to the S_8-ageing process, the initial stage of H_2S-ageing involved the formation of Cu-O compounds on the sintered nanocopper surface. Subsequently, the Cu-O compounds reacted with H_2S, leading to the formation of a mixture comprised of Cu-O and Cu-S compounds. Notably, the corrosion products generated during the H_2S-ageing process demonstrated a distinct morphology characterized by compactness and a laminar structure. These corrosion products accumulated in layers, gradually reaching a critical point where they underwent detachment from the underlying substrate in a laminar manner.

To assess the depth of corrosion penetration within the sintered samples during the H_2S-ageing process, SEM was utilized to observe the cross-sectional profiles of the 168-h H_2S-aged sintered sample. According to Fig. 9(a), the corroded surface of the sample displayed a relatively smooth morphology, indicating a limited extent of penetration corrosion. Two regions (region 1 and region 2) adjacent to the corroded surface were selected for further analysis using SEM/EDS, as illustrated in Fig. 9(a). The SEM images in Fig. 9(b) and (c) demonstrated a uniform colour distribution in both regions, suggesting the absence of detectable H_2S penetration into the internal structure of the sintered sample. EDS

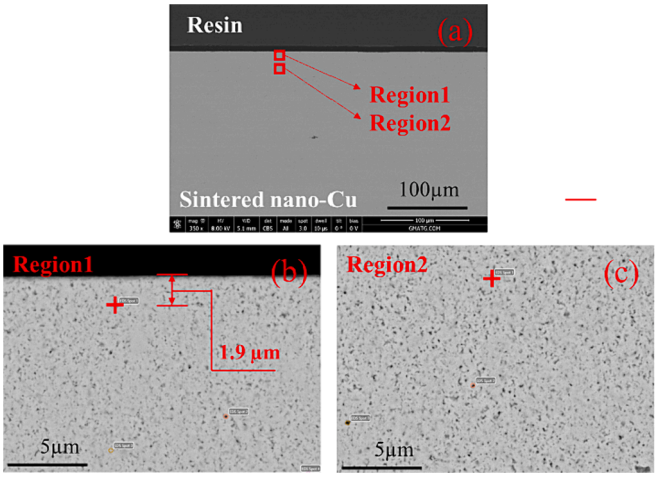

Fig. 9. Cross-sectional images of the 168-h H_2S-aged sintered samples: (a) overall view, (b) magnified view of Region 1, (c) magnified view of Region 2. Regions 1 and 2 are positioned at distances of approximately 1.9 and over 15 μm, respectively, from the surface of the sintered nanoCu substrate.

analysis was performed on selected points in Fig. 9(b) and (c), and the results are shown in Table 4. No S elements were detected in either region, indicating the absence of sulfur-based corrosion products. In the H_2S-aging process, no S element penetration into the penetration of the sintered Cu samples was detected, which contrasts with the results from S_8-aging. Additionally, the O content in both regions remained relatively low and comparable, suggesting a similar level of O.

Following the detachment of the corrosion product layer, along with the higher O content compared to the corrosion product layer on the sintered nanoCu substrate, the absence of S elements on the exposed sintered nanocopper substrate surface provided additional evidence supporting the preferential reaction of sintered nanoCu with oxygen rather than sulfur during the H_2S-ageing process.

3.1.3. *Corrosion product analysis*

Certain products formed on the sintered samples in S_8 and H_2S environments were analyzed using XRD, aiming to identify their crystallographic information, with probing depths spanning tens of micrometers. Fig. 10 shows the XRD patterns of the unaged, S_8-aged, and H_2S-aged sintered samples. Three peaks were observed for the unaged sample at approximately 43°, 50°, and 74°, which matched well with the powder diffraction file (PDF) information of Cu (PDF#85–1236). Additionally, a very weak peak near 36° corresponding to Cu_2O was observed (PDF#99–0041). In the H_2S-aged sintered sample, the intensity of the Cu_2O peak increased, while the intensity of the Cu peak slightly decreased. Similar changes were observed in the S_8-aged sample, with a more significant increase in Cu_2O peak intensity. S_8-aging led to more pronounced corrosion in sintered Cu compared to H_2S-aging, resulting in a weaker XRD peak of Cu_2O observed in the H_2S-aged samples.

XPS analysis was utilized to further verify the elemental composition of the corrosion products from each sintered sample, with probing depths limited to tens of nanometers. Fig. 11 presents the XPS spectra of the unaged, S_8-aged, and H_2S-aged samples. As shown in Fig. 11(a), the corrosion surfaces of all three sintered samples contained O, Cu, and C elements. However, the presence of S elements was only observed in the S_8-aged and H_2S-aged sintered samples. As demonstrated in Fig. 11(b), all three samples exhibited a peak at 932.3 eV, indicating the presence of metallic Cu [39]. Moreover, the spectra of the S_8-aged and H_2S-aged samples showed an additional peak at 934.4 eV, indicating the formation of CuO [40,41]. The presence of satellite peaks and their corresponding starting and ending positions further confirmed the presence of CuO. Furthermore, as shown in Fig. 11(c), the unaged sintered sample did not display a typical S 2p spectrum. In the S_8-aged and H_2S-aged sintered samples, the presence of Cu_2S was confirmed by the observed

Table 4
Cross-section elemental compositions for the different regions of the 168-h H_2S-aged sample.

Point	Cu (at%)	O (at%)	S (at%)
1	89.60	10.40	0.00
2	90.29	9.71	0.00

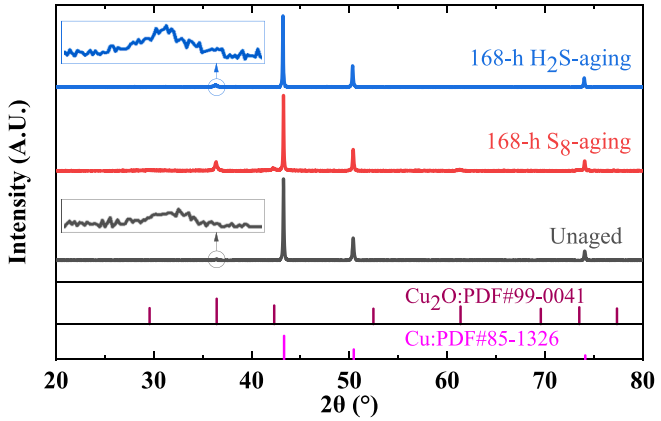

Fig. 10. XRD patterns of the sintered samples.

peaks at 162.9 and 161.7 eV for Cu^{+}-S 2p1/2 and Cu^{+}-S 2p3/2, respectively [42]. The presence of CuS was supported by the peaks at around 163.6 and 162.2 eV for Cu^{2+}-S 2p1/2 and Cu^{2+}-S 2p3/2, respectively [43,44]. Furthermore, the peaks around 168.14 and 169.24 eV confirmed the presence of SO_4^{2-} in these two sintered samples [45]. Specifically, the corrosion products that formed on the S_8-aged and H_2S-aged sintered nanocopper were similar, encompassing Cu_2O, Cu_2S, CuO, CuS, and potentially Cu_2SO_4 or $CuSO_4$.

The possible reactions involved in S_8-ageing and H_2S-ageing will be deduced based on the previous test and analysis results. When the relative humidity of the air was higher than 80 %RH, micro-droplets of water, consisting of several layers of water molecules, formed on the surface of the sintered sample [46]. These micro-droplets provided the necessary conditions for electrochemical reactions to occur. Trace amounts of oxygen from air and Cu on the sintered sample surface would dissolve in the micro-droplets, generating OH^{-} and Cu^{+} ions. The reactions involved are shown in Eqs. (4) and (5):

$$Cathode: O_2 + 2H_2O + 4e^{-} \rightarrow 4OH^{-} \quad (4)$$

$$Anode: Cu \rightarrow Cu^{+} + e^{-} \quad (5)$$

Cu^{+} reacted with OH^{-} in the solution to generate Cu_2O [37], and a small amount of Cu^{+} could react with OH^{-} to form CuO. The reactions involved were shown in Eqs. (6) and (7).

$$2Cu^{+} + 2OH^{-} \rightarrow Cu_2O + H_2O \quad (6)$$

$$2Cu^{+} + 2OH^{-} \rightarrow 2CuO + 2H^{+} + 2e^{-} \quad (7)$$

Both in S_8- and H_2S-ageing, the oxidation and sulfidation reactions of Cu occurred simultaneously. In S_8-ageing, a trace amount of S_8 molecules dissolved in water, producing S^{2-}. Cu^{+} reacted with S^{2-} to form Cu_2S, and an even smaller amount of Cu^{+} could react with S^{2-} to produce CuS. The reactions involved were shown in Eqs. (8), (9), and (10):

$$S_8 + 16e^{-} \rightarrow 8S^{2-} \quad (8)$$

$$2Cu^{+} + S^{2-} \rightarrow Cu_2S \quad (9)$$

$$Cu^{+} + S^{2-} \rightarrow CuS + e^{-} \quad (10)$$

In H_2S-ageing, H_2S molecules dissociated in water, producing HS^{-}. A trace amount of Cu^{+} reacted with HS^{-} to form Cu_2S [29], and an even smaller amount of Cu^{+} could react with HS^{-} to produce CuS. The reactions involved were shown in Eqs. (11), (12), and (13):

$$H_2S + OH^{-} \rightarrow HS^{-} + H_2O \quad (11)$$

$$2Cu^{+} + HS^{-} \rightarrow Cu_2S + H^{+} \quad (12)$$

$$2Cu^{+} + 2HS^{-} \rightarrow 2CuS + 2H^{+} + 2e^{-} \quad (13)$$

Notably, Cu_2O could further react with S_8 or H_2S to form Cu_2S [47]. The reactions involved were shown in Eqs. (14) and (15).

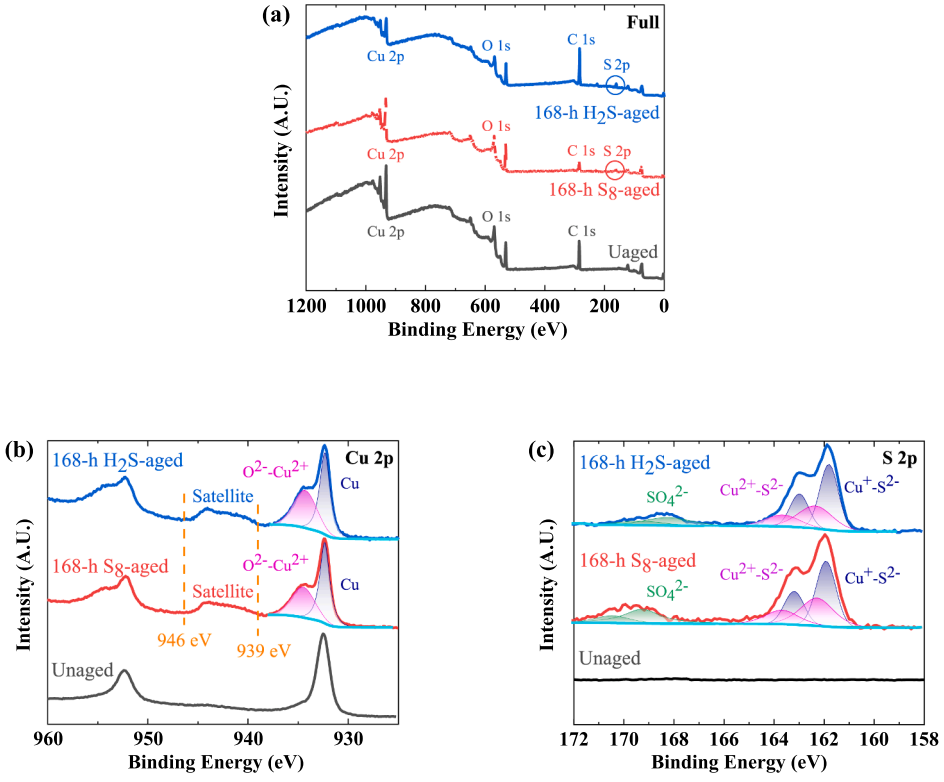

Fig. 11. XPS spectra of the sintered samples: (a) full spectrum, (b) Cu 2p spectrum, and (c) S 2p spectrum.

$$8Cu_2O + S_8 + 8H_2O + 16e^- \rightarrow 8Cu_2S + 16OH^- \quad (14)$$

$$Cu_2O + H_2S \rightarrow Cu_2S + H_2O \quad (15)$$

3.1.4. The influence of S_8- and H_2S-ageing on mechanical performance

S_8- and H_2S-induced corrosion altered the surface morphology and elemental distribution of the sintered samples, resulting in various degrees of penetration corrosion. Nanoindentation test was used to assess the impact of corrosion on the surface elastic modulus (E) and hardness (H), revealing insights into the mechanical property changes of the corroded samples.

Each sample, including the unaged, S_8-aged, and H_2S-aged samples, was subjected to 40 nanoindentation tests, with indentation positions arranged in a 4 × 10 array pattern. The indentations positions were spaced 40 μm apart in both the x and y directions, resulting in a total indentation region of 120 × 320 μm, as shown in Fig. 12(a). The nanoindentation test was conducted in accordance with the ISO 14577 standard. The test employed a test load of 50 mN and loading rate of 5 mN/s.

Table 5 presents the E and H results of the different samples following indentation testing. The mean E values of the unaged, S_8-aged, and H_2S-aged samples were 160.53, 110.94, and 117.71 GPa, respectively. The S_8-aged and H_2S-aged samples showed a decrease in E values of 30.89 % and 26.68 %, respectively, compared to the unaged sample. Similarly, the mean values of H for the unaged, S_8-aged, and H_2S-aged samples were 1.72, 1.42, and 1.51 GPa, respectively. The S_8-aged and H_2S-aged samples demonstrated a decrease in H values of 17.40 % and 12.42 %, respectively, compared to the unaged sample.

Fig. 12(b) and (c) illustrate the distributions of E and H within the test region, respectively. As shown in Fig. 12(b), distinct variations in E values were observed across the different regions of each sample surface, and more obvious discrepancies were observed in the S_8-aged samples. This was further supported by the larger standard deviation of E values in the S_8-aged samples, indicating a higher level of heterogeneity in the material surface properties resulting from the ageing process. As shown in Fig. 12(c), the surface region of the unaged sample exhibited a high degree of consistency in H values, indicating uniform hardness distribution. However, the S_8 and H_2S-ageing processes led to non-uniform distributions of surface H, with the S_8-aged samples showing more pronounced irregularity in H distribution.

Table 5
Elasticity modulus and hardness comparison of the unaged, S_8-aged, and H_2S-aged sintered samples.

Sample	Averaged E (GPa)	Standard deviation of E (GPa)	Averaged H (GPa)	Standard deviation of H (GPa)
Unaged	160.53	20.39	1.72	0.10
S_8-aged	110.94	37.10	1.42	0.60
H_2S-aged	117.71	19.44	1.51	0.22

In general, the corrosion of both S_8 and H_2S led to a reduction in the E and H of the sintered nanocopper surface, with a greater decrease rate observed in S_8 aging. Besides, the effects of both S_8 and H_2S corrosion on the surface properties of the samples were not consistent. The S_8-aged samples exhibited more significant variations in both E and H values, indicating a higher degree of heterogeneity in surface performance.

3.2. Potential of S_8 or H_2S absorption on Cu_2O

3.2.1. Surface model selection

Numerous studies have indicated that copper metal surfaces will undergo oxidation in ambient air at room temperature, leading to the formation of a Cu_2O layer [48–52]. Consistent with the prevailing body of research, the tests conducted in this study yielded identical outcomes. Fig. 10 shows Cu_2O on the surface of the unaged sample, and Fig. 11(b) indicates the absence of CuO on the unaged sample surface. As indicated in Ref. [51], within a short timeframe of 30 min, a layer of Cu_2O film would form on the Cu surface when exposed to air, measuring tens of nanometers in thickness. In a corrosive environment, the Cu_2O oxidation layer on the sintered Cu samples stored in air underwent an initial reaction with the corrosive medium present in the environment. Therefore, Cu_2O was selected for DFT research in this study.

Previous studies [34,53,54] demonstrated that the $Cu_2O(1\,1\,1)$ surface will exhibit a significantly lower surface free energy, indicating high stability. As a result, the $Cu_2O(1\,1\,1)$ surface has been frequently

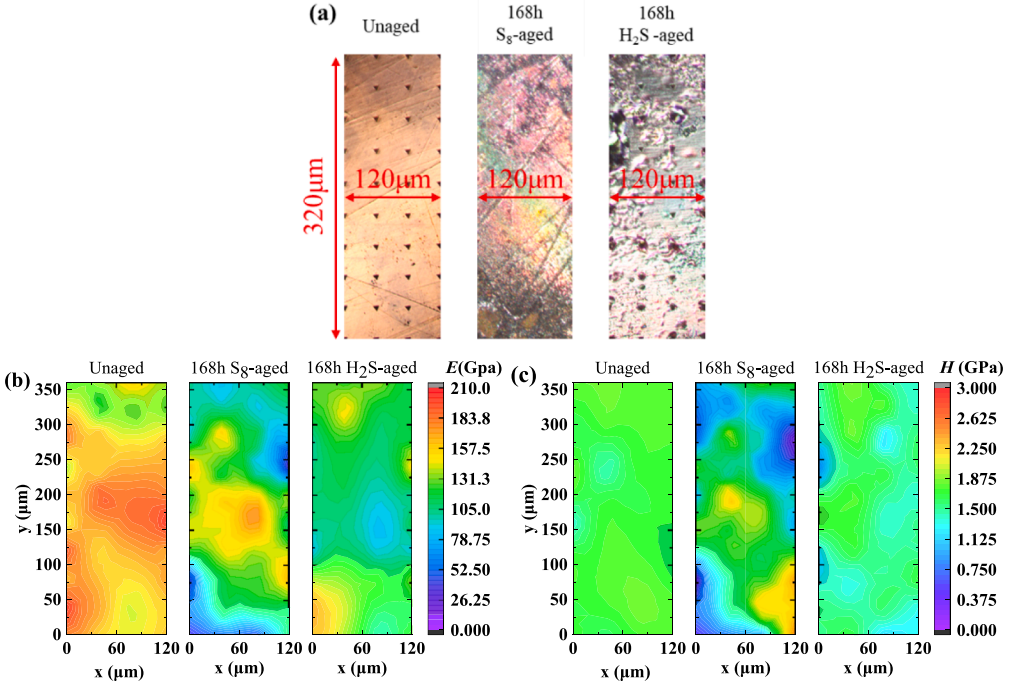

Fig. 12. (a) The morphologies of the different nanoindentation test regions, (b) elasticity modulus (E) and (c) hardness (H) distributions in each test region.

selected as an ideal model system for investigating stability, structure, and adsorption properties. Besides, the XRD spectra depicted in Fig. 10 demonstrate that both unaged and aged samples are primarily composed of the Cu_2O (1 1 1) plane, as the peak at around 36° exhibits the highest intensity. In this study, the Cu_2O(1 1 1) surface was intentionally selected and modeled with an 11-layer slab derived from a (3 × 3) supercell to determine the adsorption potential of S_8 and H_2S on Cu_2O (1 1 1). The calculated bulk lattice constants for Cu_2O were determined as 4.269 Å, which consistently aligned with the experimental values of around 4.270 Å [55,56]. As illustrated in Fig. 13, the Cu_2O(1 1 1) surface exhibited four distinctive adsorption sites, namely, the unsaturated Cu site (Cu_{usa}), the saturated Cu site (Cu_{sa}), the surface O site (O_{fi}), and the subsurface O site (O_{se}).

3.2.2. Adsorption of S_8 on Cu_2O(1 1 1)

The adsorption properties of S_8 on the Cu_2O(1 1 1) surface were investigated, taking into account four potential absorption sites including Cu_{usa}, Cu_{sa}, O_{fi}, and O_{se}. As shown in Fig. 14(a), four absorption models were used for the study, namely, S_8-Cu_{usa}, S_8-Cu_{sa}, S_8-O_{fi}, and S_8-O_{se}. An S_8 molecule was positioned on each adsorption site on the Cu_2O(1 1 1) surface, with the S_8 molecule arranged parallel to the Cu_2O(1 1 1) surface, and one S atom from the S_8 molecule positioned directly above the adsorption site at a distance of 3.5 Å.

After geometry optimization, the lowest-energy structures of the four absorption models were obtained, as shown in Fig. 14(b). The distances between S and the respective absorption sites underwent transformation from 3.5 Å to 2.177, 2.001, 3.462, and 3.68 Å. After geometry optimization, significant dissociation of the S_8 molecules and surface reconstruction of Cu_2O(1 1 1) were observed in the S_8-Cu_{usa}, S_8-Cu_{sa}, and S_8-O_{se} adsorption models. In the S_8-Cu_{usa} and S_8-Cu_{sa} adsorption models, chemical bonding interactions formed between the S atoms and their corresponding adsorption sites. Notably, in the S_8-O_{se} model, a novel bonding configuration emerged between the S atom and the Cu_{usa} site, rather than at the anticipated adsorption site (O_{se}), suggesting a non-conventional adsorption mechanism. Furthermore, the S_8-Cu_{sa} model exhibited bonding interactions between the S atom and the Cu_{usa} site, highlighting the complexity of the adsorption process and the possibility of multiple bonding configurations.

The CDD and CD were assessed to evaluate electron exchange between the atoms in the four stable models, and the results are shown in Fig. 14(c) and (d). In the CDD results, the yellow regions represented electron accumulation, while the blue regions indicated electron depletion. As illustrated in Fig. 14(c), electron transfer was observed between the two atoms involved in bond formation, resulting in electron accumulation around the bonded S atoms and electron depletion around the Cu_{usa} and Cu_{sa} sites. By contrast, the non-bonded O_{fi} and O_{se} sites remained electrically neutral without any electron gain or loss. Furthermore, an overlap of electron clouds in the S_8-Cu_{usa}, S_8-Cu_{sa}, and S_8-O_{se} stable models was observed, as shown in Fig. 14(d), which also confirmed bond formation.

To evaluate the bonding characteristics between the atoms, the DOS was calculated for the S_8-Cu_{usa} and S_8-Cu_{sa} stable models. As shown in Fig. 15(a), overlap between the d orbital of Cu_{usa} in Cu_2O(1 1 1) and the p orbital of S in S_8 was observed, indicating bond formation between S and Cu_{usa} facilitated by hybridization between the d orbital and p orbital. Similarly, as shown in Fig. 15(b), overlap between the d orbital of Cu_{sa} in Cu_2O(1 1 1) and the p orbital of S in S_8 occurred, leading to bonding between S and Cu_{sa} driven by hybridization between the d and p orbitals. Notably, the overlap area between S and Cu_{usa} was larger than between S and Cu_{sa}, implying a stronger bonding strength in S-Cu_{usa} interactions. S_8-Cu_{usa} adsorption showed a larger adsorption energy (E_{ads}) value of − 4.35 eV compared to − 3.60 eV in S_8-Cu_{sa} adsorption, as shown in Table 6. This result indicated that the Cu_{usa} site had a stronger adsorption capacity for S_8 than the Cu_{sa} site.

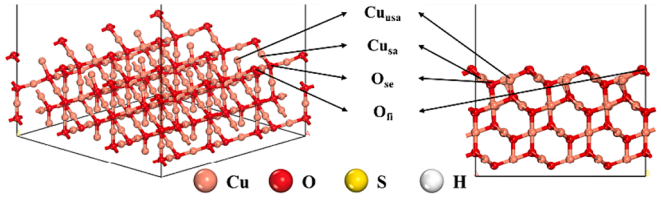

Fig. 13. Slab model of Cu_2O(1 1 1) p(3*3), indicating the four absorption sites.

3.2.3. Adsorption of H_2S on Cu_2O(1 1 1)

The adsorption behavior of H_2S on the four potential adsorption sites was investigated, and Fig. 16(a) illustrates the four absorption models, namely H_2S-Cu_{usa}, H_2S-Cu_{sa}, H_2S-O_{fi}, and H_2S-O_{se}. An H_2S molecule was positioned on each adsorption site on the Cu_2O(1 1 1) surface, with the H_2S molecule arranged parallel to the Cu_2O(1 1 1) surface, and the S atom in the H_2S molecule positioned directly above the adsorption site at a distance of 3.5 Å.

Following geometry optimization, the most energetically favorable stable structures were obtained, as presented in Fig. 16(b). The distances between the S atom and corresponding adsorption sites underwent transformation from 3.5 Å to 2.226, 3.388, 4.304, and 3.779 Å. Notably, no significant dissociation of the H_2S molecule or surface reconstruction of the Cu_2O(1 1 1) surface were observed in the post-optimization results. In the H_2S-Cu_{usa} adsorption model, chemical bonding interaction was observed between the S atom and its corresponding adsorption site (Cu_{usa}), and no new bond formation was observed in the other absorption models.

The four stable models were subjected to CDD and CD analyses, and the results are presented in Fig. 16(c) and (d). Notably, Fig. 16(c) revealed a distinct electron transfer phenomenon between the S atom in H_2S and the Cu_{usa} atom in Cu_2O(1 1 1), resulting in electron accumulation around the bonded S atom and electron depletion in the vicinity of the Cu_{usa} site. Conversely, the non-bonded Cu_{sa}, O_{fi}, and O_{se} sites showed electrical neutrality, with no observable electron migration. Moreover, as shown in Fig. 16(d), a clear overlap of electron clouds within the H_2S-Cu_{usa} stable model occurred, providing further evidence of bond formation. To assess the bonding nature between the atoms, DOS was calculated for the H_2S-Cu_{usa} stable model. As shown in Fig. 15 (c), a pronounced overlap was observed between the d orbital of Cu_{usa} in Cu_2O(1 1 1) and the p orbital of S in H_2S. This implied that bonding between S and Cu_{usa} was primarily driven by hybridization between the d orbital of Cu_{usa} and the p orbital of S. Subsequently, the adsorption energy for H_2S-Cu_{usa} adsorption was determined as − 3.78 eV (see Table 6), reflecting a favorable adsorption process with strong binding interactions between S and the Cu_{usa} site.

In summary, the adsorption behavior of the S_8 molecule on Cu_2O (1 1 1) revealed the possibility of chemical adsorption at both the Cu_{usa} and Cu_{sa} sites, with higher adsorption performance observed at the Cu_{usa} site. Conversely, the H_2S molecules could only exhibit chemical adsorption on the Cu_{usa} site of Cu_2O(1 1 1). Based on the analysis of the stable adsorption models and adsorption energies, we concluded that Cu_2O(1 1 1) exhibited a stronger adsorption capability toward S_8 compared to H_2S. For a higher amount of corrosion products and more significant mechanical performance deterioration, S_8-aging resulted in more severe corrosion to the sintered samples compared to H_2S-aging. The trends of the simulation and experimental results were consistent, confirming the accuracy of the simulation.

4. Conclusions

In this study, the ageing experiments on sintered Cu involving S_8 or H_2S were conducted first. Then, the corrosion phenomena, corrosion products, and changes in mechanical properties after corrosion were assessed using SEM/EDS, XRD, XPS, and nanoindentation techniques. Finally, DFT simulations were used to investigate the adsorption characteristics of copper oxide [Cu_2O(1 1 1)], which formed on the sintered

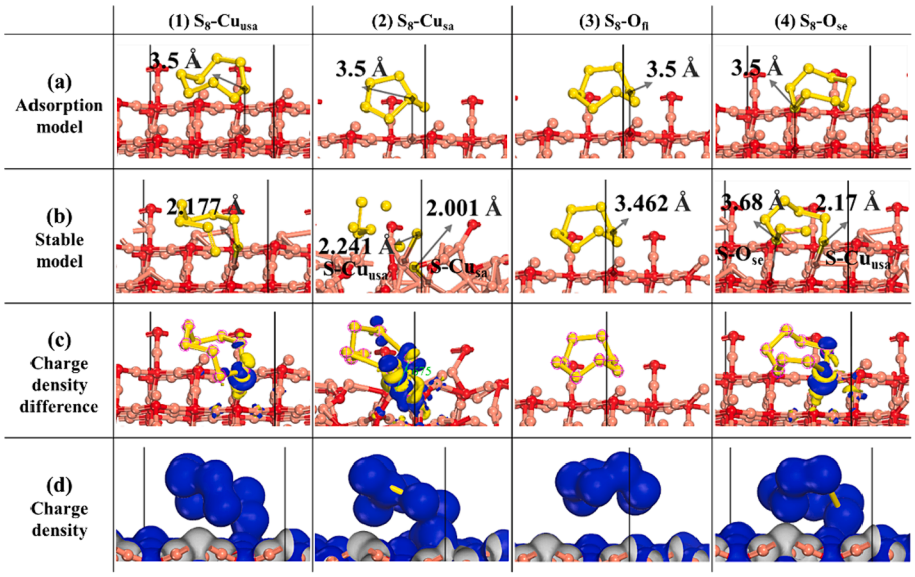

Fig. 14. Absorption model, stable model, CDD, and CD of S_8 absorption on Cu_2O.

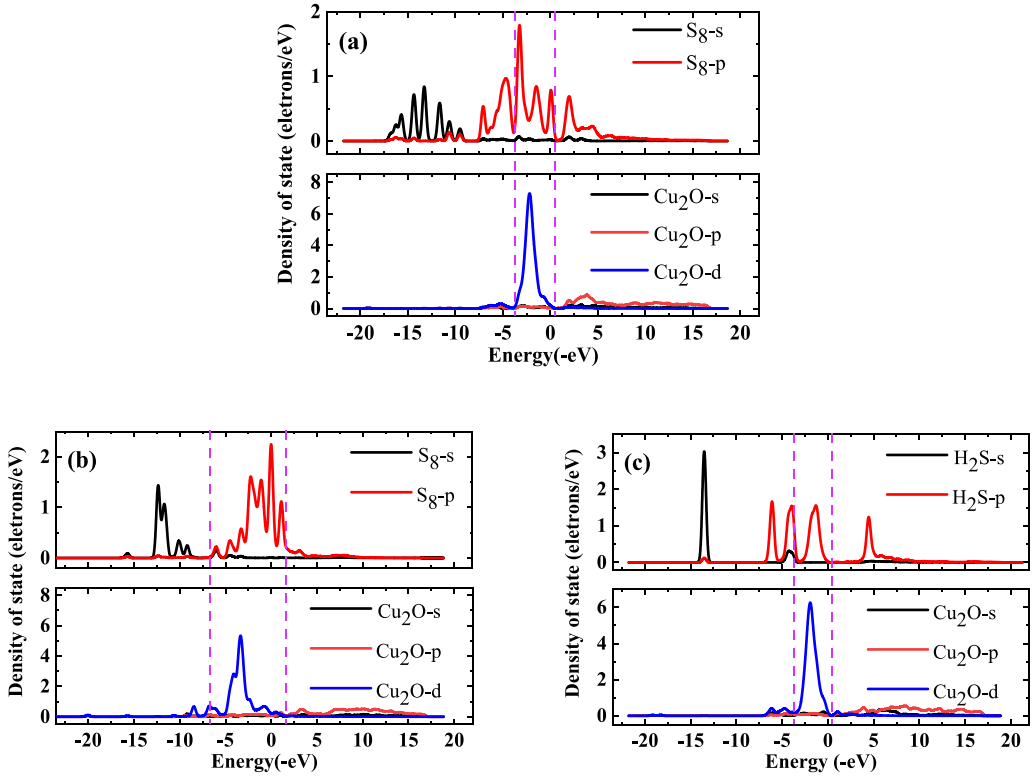

Fig. 15. DOS of the different absorption models: (a) S_8-Cu_{usa}, (2) S_8-Cu_{sa}, and (3) H_2S-Cu_{usa}.

Table 6
Adsorption energies (E_{ads}) of S_8 and H_2S for the different absorption models.

Absorption models	S_8-Cu_{usa}	S_8-Cu_{sa}	H_2S-Cu_{usa}
E_{ads} (eV)	−4.35	−3.60	−3.78

nanocopper surface, toward to S_8 or H_2S. The main conclusions of this study were as follows: (1) After undergoing 100 °C + 100 %RH + S_8 vapor ageing, the sintered sample surface exhibited the formation of loose and easily detachable corrosion products, with variations in the amount of corrosion across the different surface regions. The corrosion products primarily consisted of Cu_2O, Cu_2S, CuO, CuS, and potentially Cu_2SO_4 or $CuSO_4$. After 45 °C + 85 %RH + 100 ppb H_2S ageing, the corrosion products that formed on the sintered sample surfaces showed similar compositions as the S_8-aged samples, but with a more compact layered structure. S_8-aging resulted in more severe corrosion in the sintered samples compared to H_2S-aging, due to a higher amount of corrosion products and more significant mechanical performance deterioration. (2) The surface mechanical properties of the sintered samples were determined using nanoindentation tests. Compared to the unaged samples, both S_8- and H_2S-aged samples showed a significant reduction

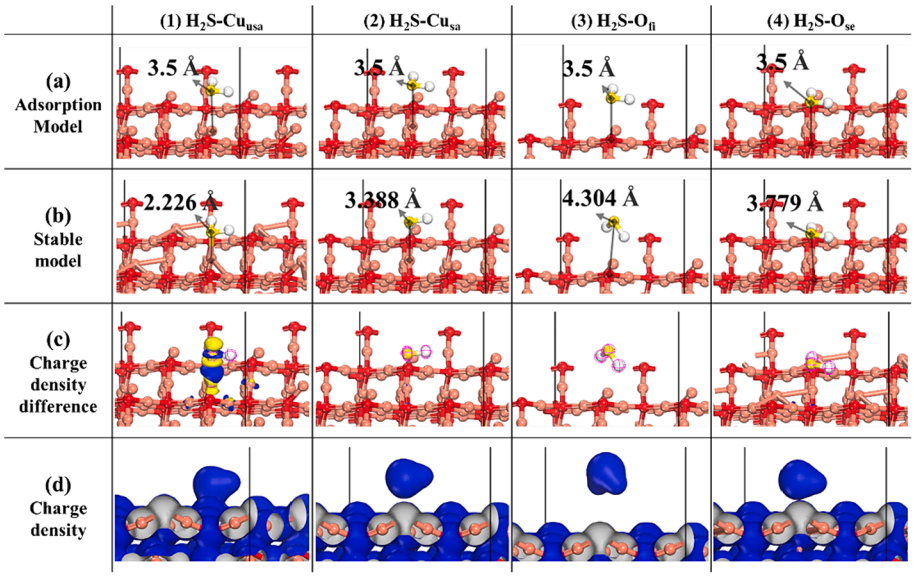

Fig. 16. Absorption model, stable model, CDD, and CD of H_2S absorption on Cu_2O.

in the elastic modulus (*E*) and hardness (*H*) values, with a more pronounced decrease observed in the S_8-aged samples. And, in the H_2S-aged samples, the reduction rates of *E* and *H* values were more consistent across different surface regions compared to the S_8-aged samples. (3) Sintered nanocopper underwent oxidation and formed a Cu_2O layer on its surface. Both the unsaturated and saturated Cu sites on Cu_2O(1 1 1) could chemically adsorb S_8, which was facilitated by the hybridization of the p orbital of S in S_8 with the d orbital of Cu in Cu_2O(1 1 1), resulting in the formation of new chemical bonds. Conversely, H_2S could only be adsorbed by unsaturated Cu sites on Cu_2O(1 1 1), also through the hybridization of the p orbital of S in H_2S with the d orbital of Cu in Cu_2O (1 1 1), leading to the formation of new chemical bonds. Cu_2O(1 1 1) exhibited a higher adsorption capacity for S_8 compared to that for H_2S. Generally, this study provided a fundamental investigation into the corrosion of sintered nanocopper in S_8 and H_2S environments, providing significant insight into the corrosion mechanisms. The findings of this study offer significant implications for the development of sulfur-resistant electronic devices, ensuring the reliability of electronic systems operating in harsh environments.

CRediT authorship contribution statement

Wei Chen: Data curation, Formal analysis, Investigation, Visualization, Writing – original draft. **Xu Liu:** Data curation. **Zhoudong Yang:** Investigation. **Dong Hu:** Investigation, Writing – review & editing. **Xi Zhu:** Supervision, Writing – review & editing. **Xuejun Fan:** Supervision. **Guoqi Zhang:** Supervision. **Jiajie Fan:** Conceptualization, Funding acquisition, Methodology, Project administration, Resources, Software, Supervision.

Declaration of competing interest

The authors declare that they have no known competing financial interests or personal relationships that could have appeared to influence the work reported in this paper.

Data availability

Data will be made available on request.

Acknowledgments

This work was partially supported by National Natural Science Foundation of China (52275559), Shanghai Pujiang Program (2021PJD002), Taiyuan Science and Technology Development Funds (Jie Bang Gua Shuai Program) and Shanghai Science and Technology Development Funds (19DZ2253400).

References

[1] W. Chen, J. Jiang, A.H. Meda, M.S. Ibrahim, G. Zhang, J. Fan, A thin and low-inductance 1200 V SiC MOSFET fan-out panel-level packaging with thermal cycling reliability evaluation, IEEE Transactions on Electron Devices 70 (5) (2023) 2268–2275.
[2] Q. Zhang, P. Zhang, A junction temperature smoothing control method for SiC MOSFETs based on the gate driving signal delay, IEEE Transactions on Industrial Electronics 71 (3) (2024) 3122–3132.
[3] C. Bai, M. Kim, Single power-conversion active-clamped AC/DC converter employing Si/SiC hybrid switch, IEEE Transactions on Industrial Electronics 71 (2) (2024) 1616–1630.
[4] Z. Wu, X. Guo, Novel coordinated control strategy for step-up/down current-source converter, IEEE Transactions on Industrial Electronics 71 (4) (2024) 3264–3274.
[5] R. Chen, C. Li, H. Fang, R. Lu, C. Li, W. Yao, W. Li, X. He, Analysis and Design for Medium Voltage Dual Active Bridge Converter Based on series-connected SiC MOSFETs, IEEE Transactions on Power Electronics 38 (12) (2023) 15620–15633.
[6] Y. Yang, Y. Wu, X. Ding, P. Zhang, Online junction temperature estimation method for SiC MOSFETs based on the DC bus voltage undershoot, IEEE Transactions on Power Electronics 38 (4) (2023) 5422–5431.
[7] H. Luo, J. Mao, C. Li, F. Iannuzzo, W. Li, X. He, Online junction temperature and current simultaneous Extraction for SiC MOSFETs with electroluminescence effect, IEEE Transactions on Power Electronics 37 (1) (2022) 21–25.
[8] R. Kumar, F. Ke, D. England, A. Summers, L. Young, A new halogen-free vapor phase coating for High Reliability & Protection of electronics in corrosive and other Harsh environments, International Conference on Electronics Packaging (ICEP) 2022 (2022) 87–88.
[9] Z. Kang, Y. He, J. Sang, H. Hirahara, D. Chen, Superhydrophobic and conductive cotton fabric composite with excellent corrosion resistance for Wearable electronics, Advanced Materials Interfaces 8 (17) (2021) 2100651.
[10] D.V. Belov, S.N. Belyaev, P.A. Yunin, Physicochemical features of biocorrosion of copper and products based on it by microfungi, Protection of Metals and Physical Chemistry of Surfaces 59 (2) (2023) 279–294.
[11] C. Qiao, M. Wang, L. Hao, X. Liu, X. Jiang, X. An, D. Li, Temperature and NaCl deposition dependent corrosion of SAC305 solder alloy in simulated marine atmosphere, Journal of Materials Science & Technology 75 (2021) 252–264.
[12] M. Wang, C. Qiao, X. Jiang, L. Hao, X. Liu, Microstructure induced galvanic corrosion evolution of SAC305 solder alloys in simulated marine atmosphere, Journal of Materials Science & Technology 51 (2020) 40–53.
[13] M. Shah, M.T.M. Ayob, N. Yaakob, Z. Embong, N.K. Othman, Effect of hydrogen sulfide and chloride on the passive film structures of stainless-steel type 316 L, Materialwissenschaft Und Werkstofftechnik 53 (2) (2022) 201–207.
[14] M. Shah, M.T.M. Ayob, N. Yaakob, Z. Embong, N.K. Othman, Comparative corrosion behaviour of austenitic 316L and duplex 2205 stainless steels:

microstructure and property evolution at highly partial pressure of H2S, Corrosion Engineering, Science and Technology 57 (1) (2022) 15–31.
[15] C. Chen, C. Choe, D. Kim, Z. Zhang, X. Long, Z. Zhou, F. Wu, K. Suganuma, Effect of oxygen on microstructural coarsening behaviors and mechanical properties of ag sinter paste during high-temperature storage from macro to micro, Journal of Alloys and Compounds 834 (2020) 155173.
[16] E. Kolbinger, S. Wagner, A. Gollhardt, O. Rämer, K.D. Lang, Corrosion behaviour of sintered silver under maritime environmental conditions, Microelectronics Reliability 88–90 (2018) 715–720.
[17] H. Gong, Y. Yao, F. Zhao, Corrosion effects on sintered nano-silver joints and the secondary biological hazards, Journal of Materials Science: Materials in Electronics 31 (10) (2020) 7649–7662.
[18] D. Hu, T.J. Gu, Z. Cui, S. Vollebregt, X.J. Fan, G.Q. Zhang, J.J. Fan, Insights into the high-sulphur aging of sintered silver nanoparticles: an experimental and ReaxFF study, Corrosion Science 192 (2021) 11.
[19] Y.H. Mei, G.Q. Lu, X. Chen, S.F. Luo, D. Ibitayo, Migration of sintered nanosilver die-attach material on alumina substrate between 250 degrees C and 400 degrees C in dry air, Ieee Transactions on Device and Materials Reliability 11 (2) (2011) 316–322.
[20] G. Lu, W. Yang, Y. Mei, X. Li, G. Chen, X. Chen, Mechanism of migration of sintered nanosilver at high temperatures in dry air for electronic packaging, IEEE Transactions on Device and Materials Reliability 14 (1) (2014) 311–317.
[21] G.-Q. Lu, C. Yan, Y. Mei, X. Li, Dependence of electrochemical migration of sintered nanosilver on chloride, Materials Chemistry and Physics 151 (2015) 18–21.
[22] Y.N. Zheng, Y.H. Mei, F. Long, X. Li, C.Y. Yan, G.Q. Lu, Electrochemical migration of sintered nanosilver under chloride-containing thin electrolyte layer for power electronic packaging, CORROSION 72 (4) (2016) 547–559.
[23] D. Minzari, M.S. Jellesen, P. Møller, R. Ambat, Morphological study of silver corrosion in highly aggressive sulfur environments, Engineering Failure Analysis 18 (8) (2011) 2126–2136.
[24] R. Riva, C. Buttay, B. Allard, P. Bevilacqua, Migration issues in sintered-silver die attaches operating at high temperature, Microelectronics Reliability 53 (9) (2013) 1592–1596.
[25] B. Liao, H. Wang, L. Kang, S. Wan, X. Quan, X. Zhong, X. Guo, Electrochemical migration behavior of low-temperature-sintered ag nanoparticle paste using water-drop method, Journal of Materials Science: Materials in Electronics 32 (5) (2021) 5680–5689.
[26] D. Li, Y. Mei, Y. Xin, Z. Li, P.K. Chu, C. Ma, G.Q. Lu, Reducing migration of sintered ag for power Devices operating at high temperature, IEEE Transactions on Power Electronics 35 (12) (2020) 12646–12650.
[27] M. Nishimoto, R. Tokura, M.T. Nguyen, T. Yonezawa, Copper materials for low temperature sintering, MATERIALS TRANSACTIONS 63 (5) (2022) 663–675.
[28] T.F. Chen, K.S. Siow, Comparing the mechanical and thermal-electrical properties of sintered copper (Cu) and sintered silver (Ag) joints, JOURNAL OF ALLOYS AND COMPOUNDS 866 (2021) 158783.
[29] T.T.M. Tran, C. Fiaud, E.M.M. Sutter, Oxide and sulphide layers on copper exposed to H2S containing moist air, Corrosion Science 47 (7) (2005) 1724–1737.
[30] T.N. Wassermann, O. Schilling, K. Müller, A. Rossin, J. Uhlig, A new high-voltage H2S single noxious gas reliability test for power modules, Microelectronics Reliability 100–101 (2019) 113468.
[31] H. Tang, Z. Qu, L. Wang, H. Ye, X. Fan, G. Zhang, Correction: liquid-phase exfoliated SnS as a semiconductor coating filler to enhance corrosion protection performance, Physical Chemistry Chemical Physics 22 (21) (2020) 12321.
[32] D. Kumar, V. Jain, B. Rai, Imidazole derivatives as corrosion inhibitors for copper: a DFT and reactive force field study, Corrosion Science 171 (2020) 108724.
[33] X. Liu, S. Li, J. Fan, J. Jiang, Y. Liu, H. Ye, G. Zhang, Microstructural evolution, fracture behavior and bonding mechanisms study of copper sintering on bare DBC substrate for SiC power electronics packaging, Journal of Materials Research and Technology 19 (2022) 1407–1421.
[34] R. Zhang, H. Liu, J. Li, L. Ling, B. Wang, A mechanistic study of H2S adsorption and dissociation on Cu2O(111) surfaces: thermochemistry, reaction barrier, Applied Surface Science 258 (24) (2012) 9932–9943.
[35] S. Chen, S. Sun, Y. Ma, B. Lian, S. Hu, Effects of coverage and solvent on H2S adsorption on the Cu(100) surface: a DFT study, Surface and Interface Analysis 47 (5) (2015) 565–571.
[36] Y. He, X. Zhao, C. Chen, H. Yu, First principles molecular dynamics simulations of H2S dissociation on fe (111) in aqueous environments, Applied Surface Science 554 (2021) 149618.
[37] M. Watanabe, M. Takaya, T. Handa, J. Sakai, Characterisation of corrosion products formed on copper exposed at indoor and outdoor sites with high H2S concentrations, Corrosion Engineering, Science and Technology 48 (6) (2013) 418–425.
[38] J. Becker, J. Pellé, S. Rioual, B. Lescop, N. Le Bozec, D. Thierry, Atmospheric corrosion of silver, copper and nickel exposed to hydrogen sulphide: a multi-analytical investigation approach, Corrosion Science 209 (2022) 110726.
[39] C.R. Anderson, R.N. Lee, J.F. Morar, R.L. Park, Comparison of APS and FRESCA core level binding energy measurements, Journal of Vacuum Science and Technology 20 (3) (1982) 617–621.
[40] F.M. Capece, V.D. Castro, C. Furlani, G. Mattogno, C. Fragale, M. Gargano, M. Rossi, "Copper chromite" catalysts: XPS structure elucidation and correlation with catalytic activity, Journal of Electron Spectroscopy and Related Phenomena 27 (2) (1982) 119–128.
[41] H. Sun, O.A. Zelekew, X. Chen, Y. Guo, D.-H. Kuo, Q. Lu, J. Lin, A noble bimetal oxysulfide CuVOS catalyst for highly efficient catalytic reduction of 4-nitrophenol and organic dyes, RSC Advances 9 (55) (2019) 31828–31839.
[42] L. Jin, L. Cai, D. Chen, W. Wang, H. Shen, F. Zhang, Efficient silicon solar cells applying cuprous sulfide as hole-selective contact, Journal of Materials Science 54 (19) (2019) 12650–12658.
[43] S. Tarachand, N.P. Hussain, Y.K. Lalla, A. Kuo, V.G. Lakhani, U. Sathe, G. S. Deshpande, Okram, thermoelectric properties of ag-doped CuS nanocomposites synthesized by a facile polyol method, Physical Chemistry Chemical Physics 20 (8) (2018) 5926–5935.
[44] N. Karikalan, R. Karthik, S.-M. Chen, C. Karuppiah, A. Elangovan, Sonochemical synthesis of sulfur doped reduced graphene oxide supported CuS Nanoparticles for the non-enzymatic glucose sensor applications, Scientific Reports 7 (1) (2017) 2494.
[45] C. Wang, C. Zhang, Y. Zhao, X. Yan, P. Cao, Poisoning effect of SO2 on honeycomb cordierite-based Mn–Ce/Al2O3Catalysts for NO reduction with NH3 at low temperature, Applied Sciences 8 (1) (2018) 1–13.
[46] A.L. Sumner, E.J. Menke, Y. Dubowski, J.T. Newberg, R.M. Penner, J. C. Hemminger, L.M. Wingen, T. Brauers, B.J. Finlayson-Pitts, The nature of water on surfaces of laboratory systems and implications for heterogeneous chemistry in the troposphere, Physical Chemistry Chemical Physics 6 (3) (2004) 604–613.
[47] K. Mikami, Y. Kido, Y. Akaishi, A. Quitain, T. Kida, Synthesis of Cu2O/CuO nanocrystals and their application to H2S sensing, Sensors 19 (1) (2019) s19010211.
[48] J. Iijima, J.W. Lim, S.H. Hong, S. Suzuki, K. Mimura, M. Isshiki, Native oxidation of ultra high purity cu bulk and thin films, Applied Surface Science 253 (5) (2006) 2825–2829.
[49] Z. Liu, Y. Bando, Oxidation behaviour of copper nanorods, Chemical Physics Letters 378 (1) (2003) 85–88.
[50] C. Gattinoni, A. Michaelides, Atomistic details of oxide surfaces and surface oxidation: the example of copper and its oxides, Surface Science Reports 70 (3) (2015) 424–447.
[51] Y. Unutulmazsoy, C. Cancellieri, M. Chiodi, S. Siol, L. Lin, L.P.H. Jeurgens, In situ oxidation studies of cu thin films: growth kinetics and oxide phase evolution, Journal of Applied Physics 127 (6) (2020) 065101.
[52] P.K. Krishnamoorthy, S.C. Sircar, Effect of cold working and annealing on oxidation rates of copper in dry air at room temperature, Corrosion 24 (12) (2013) 407–410.
[53] X. Yu, X. Zhang, S. Wang, G. Feng, A computational study on water adsorption on Cu2O(111) surfaces: the effects of coverage and oxygen defect, Applied Surface Science 343 (2015) 33–40.
[54] X. Yu, C. Zhao, T. Zhang, Z. Liu, Molecular and dissociative O2 adsorption on the Cu2O(111) surface, Physical Chemistry Chemical Physics 20 (31) (2018) 20352–20362.
[55] R. Restori, D. Schwarzenbach, Charge density in cuprite, Cu2O, Acta Crystallographica Section B 42 (3) (1986) 201–208.
[56] M.A. Nygren, L.G.M. Pettersson, H2O Interaction with the Polar Cu2O(100) Surface: a theoretical study, The Journal of Physical Chemistry 100 (5) (1996) 1874–1878.